Renewable Energy 118 (2018) 627–643

Contents lists available at ScienceDirect

Renewable Energy

journal homepage: www.elsevier.com/locate/renene

Co-located offshore wind and tidal stream turbines: Assessment of energy yield and loading

D. Lande-Sudall [a, *], T. Stallard [b], P. Stansby [b]

[a] Western Norway University of Applied Sciences, Department of Mechanical and Marine Engineering, Inndalsveien 28, 5020, Bergen, Norway
[b] University of Manchester, School of Mechanical, Aerospace and Civil Engineering, Oxford Road, Manchester, M13 9PL, UK

ARTICLE INFO

Article history:
Received 30 September 2016
Received in revised form
21 September 2017
Accepted 21 October 2017

Keywords:
Co-location
Offshore wind farms
Tidal stream arrays
Hybrid
Environmental loads
Energy yield

ABSTRACT

Co-location of wind and tidal stream turbines provides opportunity for improved economic viability of electricity generation from these resources relative to projects exploiting each resource separately. Here co-deployment is assessed in terms of energy generation and loading of support structures. Energy yield is modelled using an eddy viscosity wake model for wind turbines and superposition of self-similar wakes for tidal turbines. A case-study of the Inner Sound of the Pentland Firth is considered. For 3.5 years of coincident resource data, 12 MW wind capacity co-located with a 20 MW tidal array results in a 70% increase in energy yield, compared to operating the tidal turbines alone. Environmental loads are modelled for a braced monopile structure supporting both a wind and tidal turbine, as well as for each system in isolation. Peak loading of the combined system is found to be driven by wind loads with greatest overturning moment occurring with the wind turbine operating at close to rated-speed and the tidal turbine close to its shutdown speed. Mean loads vary across the tidal array by 6% indicating no significant shielding effects are gained by co-locating in more sheltered regions of the array.

1. Introduction

In-line with the commitments signed by the 175 countries of the 2015 Paris Agreement recognising the need to significantly cut global greenhouse gas emissions [1], further expansion of large offshore wind farm deployments are expected. In the UK, electricity generated from offshore wind is currently around 17 TWh/yr [2] and is anticipated to reach over 90 TWh/yr[1] by 2030. However, the cost of electricity from offshore wind has failed to decrease as expected through experience alone [4]. Many planned wind farm locations require deployment in water depths greater than 30 m where traditional support structures may no longer be feasible and the required systems may have higher capital cost. As such levelised cost of energy is likely to remain higher than for gas or coal generation and large scale deployment of wind is likely to rely on continued government incentives. Deployment of other renewable technologies, such as solar and wave alongside wind farms (co-location) have been proposed as methods of cost reduction of electricity generation (e.g. Tina et al. [5] and Gao et al. [6]). In this study, co-location of offshore wind turbines with farms of tidal stream turbines is considered. Tidal stream turbines are a less mature technology than offshore wind or solar. However tidal arrays are currently being installed and there is the potential in the UK to generate an estimated 18 TWh/yr from the tidal stream resource [7] and average power of more than 2 GW from the Pentland Firth alone [8]. Co-location enables shared use of electrical infrastructure and, potentially, of support structures. There may also be benefits in terms of reduced variability of power from a co-located farm as opposed to operating a wind or tidal farm in isolation. Existing offshore wind farms have typically been installed in locations with low tidal stream velocities. As such, this study addresses co-location of wind turbines at sites being developed for tidal stream arrays, since a strong tidal stream resource will be required for tidal generation.

To assess economic viability of alternative design options at a preliminary stage of development, it is informative to assess how factors which directly influence revenue and capital expenditure may differ. Revenue from renewable energy projects is dependent on annual energy production and the accuracy with which this may be forecast is clearly vital. Capital cost is dependent on many factors

* Corresponding author.
E-mail addresses: david.lande-sudall@hvl.no (D. Lande-Sudall), tim.stallard@manchester.ac.uk (T. Stallard).

[1] Based on [3] prediction of 33 GW of installed capacity by 2030 and an average capacity factor of 33%.

https://doi.org/10.1016/j.renene.2017.10.063

including dimensions, complexity and number of support structures, as well as site-specific installation costs. To this end, a model of the energy yield from co-located wind and tidal turbines is first presented, along with evaluation of time varying power for a case-study farm comprising 12 MW offshore wind power capacity co-located with 20 MW tidal capacity, situated in the Inner Sound of the Pentland Firth, Scotland. It is noted that the methodology could be applied to any site of interest. For the tidal stream array, the influence of a yaw operating strategy and shutdown criterion based on both current speed and significant wave height, H_s, is considered, since these directly influence yield and tidal turbine complexity. The second part of this paper assesses the environmental loads acting on a hybrid support structure for a wind and tidal stream turbine, since such loads affect structural dimensions. The loads are compared against those acting on support structures for wind and tidal turbines in isolation.

2. Wind farm energy yield model

AWS OpenWind [9] with a standard eddy-viscosity wake model [10] is used to model wind farm energy yield. A generic 3 MW power curve is specified for each turbine, with a rotor diameter of 100 m, rated speed of 12 m/s and shutdown set at 25 m/s. The thrust curve was from a 3 MW Vestas V90 wind turbine [11] in order to define the momentum extraction in the wake model. The wind turbines are assumed to operate with 100% availability, with no downtime due to faults or maintenance. A power matrix, specific to the farm layout and dependent on wind heading, is generated. This is used as a look-up table against hourly wind resource data to obtain time-varying power output.

Numerical Weather Prediction (NWP) data of wind resource at 10 m height is available from the UK Met Office UKV model [12] in a 6-hourly time-series for the periods 01 Jan 2012–30 Nov 2012 and 01 Jan 2013–24 Jun 2015 and at an approximately 1.5 km spatial resolution. This approximately 3.5 years of data is too short to account for the wind power variability over the life-time of the farm (e.g. decadal variability [13]). However, the approach used herein can also be applied to longer time-series, as more data becomes available. This analysis therefore provides an indication of the relative magnitude of wind to tidal energy yield, the power variability, and when used for analysing loads, the operational conditions of the turbines during peak load events. Since this dataset is at relatively coarse spatial and temporal resolution, a linear measure-correlate-predict (MCP) approach has been applied to the UKV data, using wind data from an hourly, 400 m resolution mesoscale Weather Research and Forecasting (WRF) model [14,15] employed over the Pentland Firth region. The WRF model is considered to provide a more accurate representation of the undisturbed wind speeds at the site and was configured according to [16] who previously validated the model against measured data from five met stations around the Pentland Firth. Initial and boundary conditions were from National Centres for Environmental Prediction (NCEP) Final (FNL) Global Analysis data at $1^\circ \times 1^\circ$ spatial and 6-hourly temporal resolutions [17]. Five telescopic nested-domains, each of 78×78 compute nodes provided an outer domain resolution of 32.4 km, increasing in ratios of 3:1 to an inner domain resolution of 400 m on plan. In the vertical axis, 45 η levels were specified with ten levels within the lowest 250 m.

The WRF model has been run for an aggregate period of eight weeks and wind speed at 10 m level extracted to correlate with the UKV model data. The intervals considered comprised two, non-overlapping 14-day periods and four, non-overlapping 7-day periods (see Fig. 1). Each interval was selected such that the wind speed occurrence represented annual occurrence statistics defined

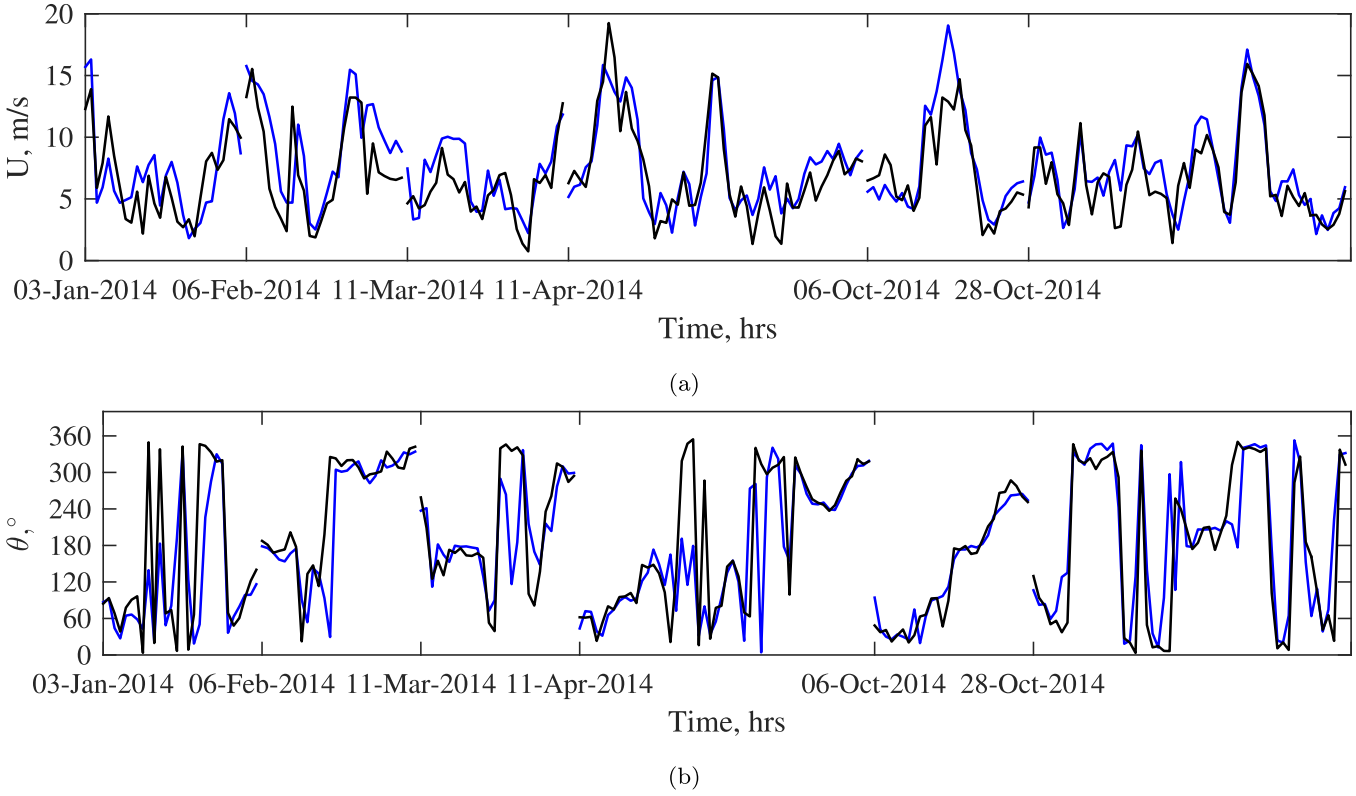

Fig. 1. Hourly time-series of wind speed (a) and direction (b) at 10 m elevation from both UKV (black) and WRF (blue). The figure shows data for six separate time-intervals, with the start date of each shown on the x-axis. (For interpretation of the references to colour in this figure legend, the reader is referred to the web version of this article.)

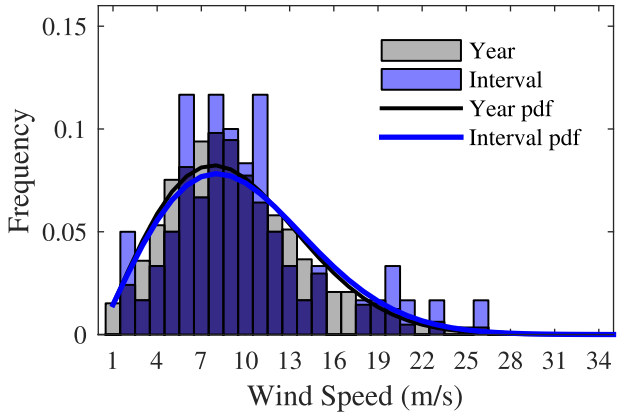

Fig. 2. Weibull distributions for the year 2014 and for the fortnight commencing 10/04/2014 for which wind speed occurrence is comparable to the annual. Data is from the uncorrected-UKV model at the target site.

by the minimum value of the following six error indicators: Difference of mean wind speed; root-mean-square error (RMSE) of wind speed histograms; RMSE of probability distribution functions (PDFs) of wind speed; Average RMSE of the 12-sector wind rose; RMSE of PDF-fit to wind speed histogram; and difference in energy yield from a single turbine operating under each distribution. The occurrence probability for the period beginning 10 April 2014 are shown against the annual occurrence probability and corresponding Weibull distribution in Fig. 2.

Various methods for correcting the coarser but longer time-period of UKV data to the eight weeks of WRF data have been evaluated, including; linear regression, a standard linear MCP method (eqn. (1)) and a non-parametric method [18]. The MCP method predicted both extreme high and low wind speeds most accurately, important for estimation of extreme loads and improved the root-mean-squared error between correction and WRF data from 1.85 m/s of the uncorrected data to 1.69 m/s once corrected.

$$\widehat{U}(\theta)_{ukv} = \alpha_\theta U(\theta)_{ukv} + \beta_\theta \tag{1}$$

where $U(\theta)_{ukv}$ is the un-corrected and $\widehat{U}(\theta)_{ukv}$ the corrected UKV 10 m wind speeds, α_θ and β_θ are constants found by linear regression of the 8 week interval of coincident un-corrected UKV and WRF wind speed data for each 30° direction bin, θ.

3. Tidal farm energy yield model

Methods for modelling of wind turbine wake interactions within farms are reasonably well established. The presence of a bounding free-surface means that although there are some similarities for farms of tidal stream turbines, analogous approaches aren't directly transferable and to date, there are few validated approaches available. The range of methods being investigated include semi-empirical models to CFD of various levels of complexity. One approach is to include actuator disc representations of turbines embedded into shallow water solvers to represent energy extraction from fences of multiple turbines [19]. Reynolds-averaged Navier Stokes-Blade Element Momentum (RANS-BEM) CFD models have also been used to model small arrays of turbines and resolve device scale characteristics, such as [20,21]. However, both are relatively computationally expensive and so a quick, reliable approach, similar to the Ainslie [10] or Jensen [22] models for wind, is desirable for rapid evaluation of tidal energy yield [23]. A computationally efficient method is the superposition of semi-empirical descriptions of self-similar wakes. In experiments by Stallard et al. [24] of a 1/70th geometry, Froude scaled tidal turbine, the authors show that beyond six diameters (D_t) downstream of the rotor plane, the vertical profile of velocity deficit becomes almost a depth-averaged plane wake with a transverse profile following a self-similar Gaussian form. The centreline velocity deficit, ΔU_{max} is then proportional to $x^{-1/2}$ (eqn. (2)) and half wake width, $y_{1/2}$ proportional to $x^{1/2}$ (eqn. (3)).

$$\frac{\Delta U_{max}}{U_0} = -0.126 + 0.8639(x_D)^{-\frac{1}{2}} \tag{2}$$

$$y_{1/2} = 0.5 + 0.4118(x_D)^{\frac{1}{2}} \tag{3}$$

where x_D is the ratio of downstream distance to diameter and $y_{1/2}$ is the width of the wake at $\frac{1}{2}\Delta U_{max}$.

These relationships were obtained for a single turbine located within a shallow turbulent channel flow of depth 1.67 D_t and with mean turbulence intensity of 12% and some variation is expected with these parameters [21]. The local velocity deficit, ΔU in the wake due to a single turbine, i (eqn. (4)), is then:

$$\Delta U_i = \Delta U_{max} \exp\left(\frac{-ln(2)y_r^2}{y_{1/2}^2}\right) \tag{4}$$

where y_r is the distance from the centreline relative to the disc radius.

The velocity deficits from a single row of k turbines are then superposed as in equation (5), giving the overall reduced velocity deficit of the combined wake, ΔU_w.

$$\Delta U_w = \sum_{i=1}^{k} \Delta U_i \tag{5}$$

where Δ has been used to represent velocity deficits, i.e. $\Delta U_w = U_0 - U_w$.

For multiple rows of turbines, deficit superposition is treated in a streamwise parabolic manner as in Stansby and Stallard [25] (see Fig. 3). The deficit, ΔU_r at distance, x_r behind the r-th row of downstream turbines, is due to the superposition of all upstream turbine wake deficits. In other words, the deficit from the first row of turbines provides the onset flow profile to the second row, with the deficit of the second row providing the onset flow for the third row and so on. Hence eqn. (5) can be applied as:

$$\Delta U_r(x_r, y_r) = \Delta U_{r-1}(x_r, y_r) + \sum_{i=1}^{n} \Delta U_i(x_r, y_r); \quad x_r \geq 6\, D_t \tag{6}$$

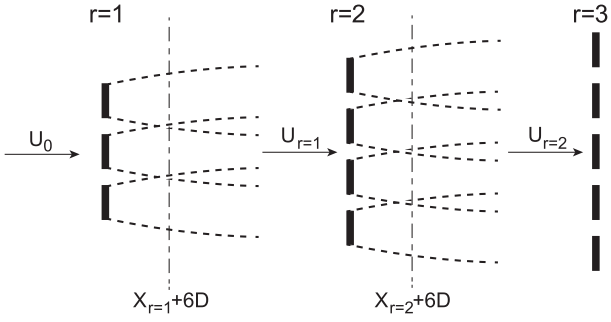

Fig. 3. Parabolic treatment of wake superposition.

where ΔU_r is the velocity deficit at x_r, y_r due to all turbines in rows upstream of and including row r, ΔU_{r-1} is the velocity deficit due to all turbines in rows upstream of and including row $r-1$, and ΔU_i is the velocity deficit for all turbines, $i = 1, n$, in row r; x_r is the perpendicular downstream distance (aligned with bulk flow direction) from row r; y_r is orthogonal to x_r.

Variation of global blockage between rows can be accounted for by applying conservation of volume flux at each streamwise row positions. This approach provides good agreement to measurements of the wake of scaled rotors [25]. A local blockage correction can also be applied [26], however neither approach to blockage correction is applied in the present study since global blockage is negligible and transverse turbine spacing is relatively large. For downstream turbines, the onset flow is due to the wake of upstream turbines with turbulence intensity differing from the ambient flow. Turbulence of the wake differs from the ambient flow, with higher turbulence intensity occurring over the near-wake region and decaying with distance downstream. For the relatively large turbine spacings considered here (transverse spacing 1.5 D_t, streamwise greater than 8 D_t), turbulence intensity is assumed to recover to the same value as the ambient flow (e.g. Stallard et al. [24]) and this approach of superposition of semi-empirical wakes has been shown to be suitable [25].

Applying the superposition method, the velocity deficit field at hub-height across the array can be established for a specific turbine layout and range of inflow headings. The area-weighted average of hub-height velocity, weighted by a thin vertical strip of width, w across the swept area of the rotor, A_D is used for calculating the power at each turbine and obtained as in equation (7).

$$U_{avg} = \frac{1}{A_D}\sum_{i}^{n} U_i dA_i \tag{7}$$

where $dA_i \approx 2w\sqrt{R^2 - r_i^2}$ for n number of small strips and radial height, r_i of the i-th strip.

3.1. Tidal resource data

There are limited open-access sources of flow velocity data for sites considered suitable for tidal stream turbine deployment. Hourly time-series of tidal resource data from the Forecasting Ocean and Assimilation Model (FOAM) [27], provided by the E.U. Copernicus Marine Environment Monitoring Service, at 7 km horizontal resolution was previously used by Sudall et al. [28]. However the low spatial resolution meant that both mean and maximum current speeds were under-predicted, leading to unrealistically low tidal turbine capacity factors being calculated for the site. In this study, a 2D ADvanced CIRCulation model (ADCIRC) used in Adcock et al. [8] with 15-min temporal and 150 m spatial resolution has provided northing and easting components of current velocity. Data from the node (58.6577°, −3.1272°) nearest to the centre of the array is taken for the seven month period between 01

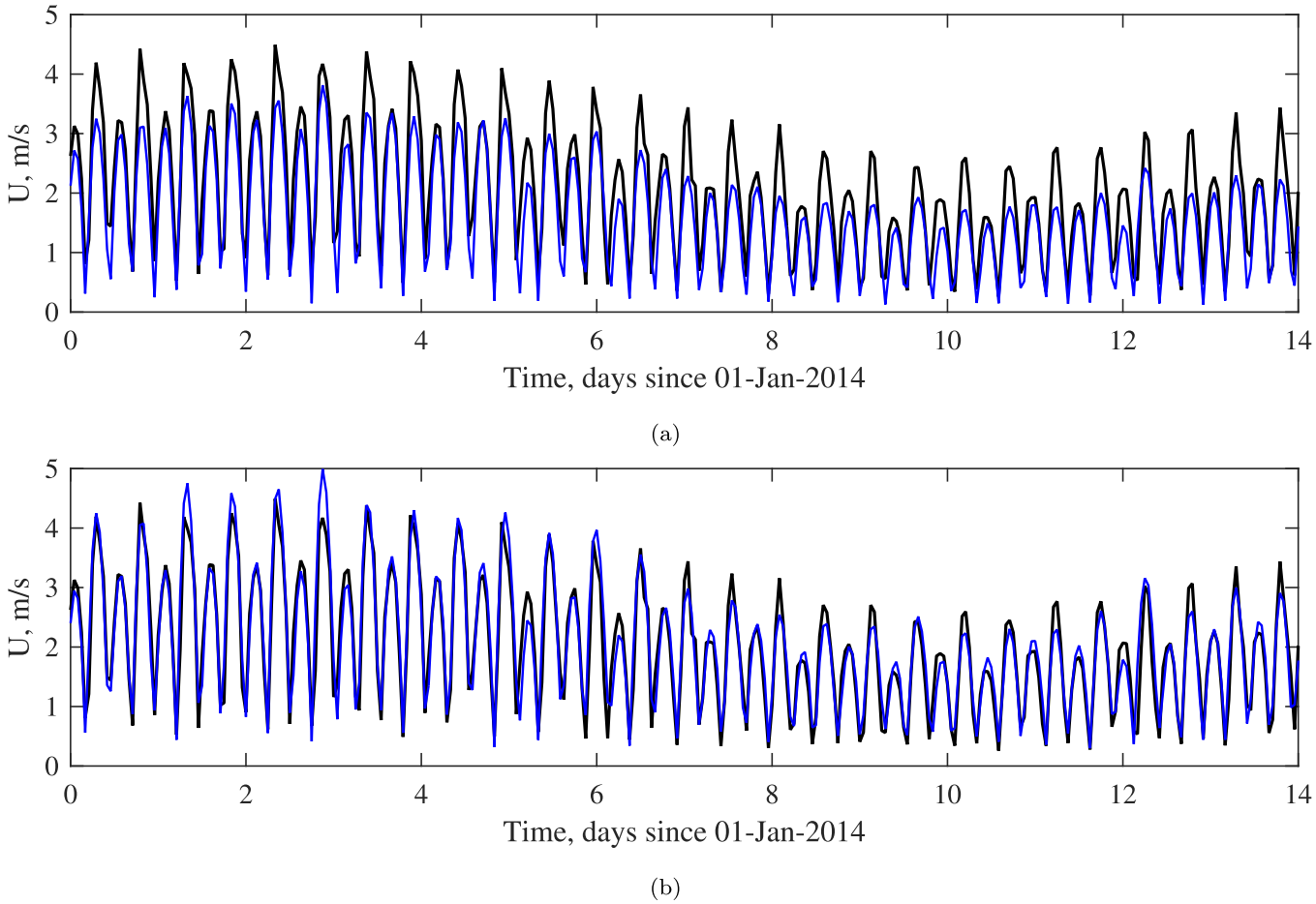

Fig. 4. Current magnitude for un-correct FOAM data (blue) and ADCIRC (black) (a) and for MCP-corrected FOAM (blue) and ADCIRC (black), (b). (For interpretation of the references to colour in this figure legend, the reader is referred to the web version of this article.)

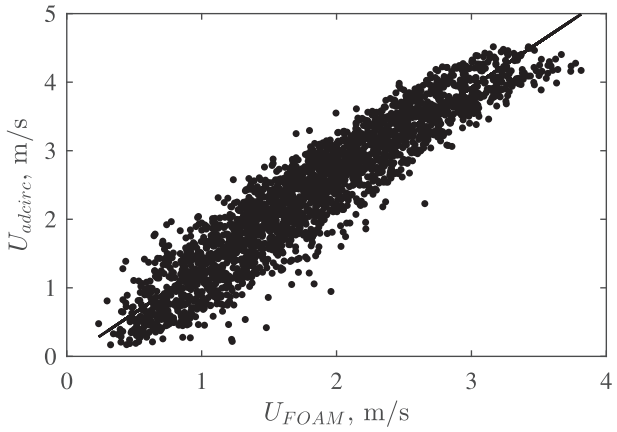

Fig. 5. Linear regression for direction sector 105°–135°.

Jan 2014–29 Aug 2014 and is compared to the same period of data from FOAM in Fig. 4a).

The ADCIRC model captures higher peak current velocities, more representative of those seen from ADCP measurement campaigns of the currents in the Pentland Firth [29]. The same linear MCP method (Fig. 5) as used for the wind data analysis, has been used to correlate the ADCIRC data to the FOAM data (Fig. 4b)). Application of MCP improved the R-squared correlation coefficient from 0.57 to 0.91. The direction-dependent correlation functions are then applied to the three and a half year period of FOAM data.

3.2. Tidal turbine specification

It is widely recognised that turbines must be sized appropriately for the resource such that the energy generated, hence revenue accrued, justifies the installed capacity. A generic power curve is defined specifying rated power and maximum power coefficient, $C_{p_{max}}$ for a rotor of diameter $D_t = 18$ m, typical of prototype turbines operating in 30 m water depth. The cut-in speed is defined at the power required to overcome the generator resistive torque (difference between mechanical and electrical power), approximately 8% of the rated power, P_{rate}. The rated speed, U_{rate} then varies with maximum power coefficient, $C_{p_{max}}$ and P_{rate} with shut-down speed set at 5 m/s. To be consistent with the wind turbines, the tidal turbines have also been assumed to operate with 100% availability.

In order to determine a suitable size turbine for the site, energy yield of a small array was evaluated for a range of rated power and maximum power coefficients. The array comprised a rectilinear layout of 2 rows of 5 turbines with Y = 1.5 D_t lateral spacing. Both X = 10 D_t and 20 D_t longitudinal spacings were tested with results shown for X = 10 D_t in Fig. 6. Since project developers are expected to seek both good annual energy yield and high capacity factor (CF) a rated power of 1 MW and maximum power coefficient of 0.44 are selected, giving a CF of 0.39 for 10 D_t spacing. This is comparable to typical capacity factors seen for offshore wind farms, close to 0.35 [30]. Fig. 7 shows that for 28.8% of the time, the current velocities are below cut-in speed of the turbine. This contrasts with the wind speed distribution at the same location, which is below the wind turbine cut-in speed for around 2% of the time.

3.3. Tidal yaw control strategy

The analysis of the preceding section was based on application of a continuous yaw strategy, analogous to that used in wind turbines. Although a continuous strategy is being used by the TEL Delta Stream device [31], it is complex to implement in the underwater environment and alternative yaw control strategies could be adopted, such as slack-tide yaw (e.g. Alstom/GE DEEP-Gen IV [32]) or fixed (e.g. MCT SeaGen [33]). For a fixed yaw strategy, the nacelle remains fixed but pitching of the blades enables the turbine to generate power on both the ebb and flood of a bi-directional tide. In slack-tide yaw, the turbine nacelle only yaws during a slack tide, defined in the model as the local minimum in current velocity ($d^2U/dt^2 > 0$). The turbine is orientated to the heading which will maximise energy yield during the subsequent half tidal period (i.e. the time between two slack tides) and this is based on the power curve of a single turbine. In reality, this strategy would require accurate prediction of the heading for the next half-tidal cycle.

Variability in current heading during a half tidal period means the turbine rotor plane will be subject to oblique inflow angles for both the slack-tide and fixed orientation strategies. For small angles, $\phi_t \leq \pm 7.5°$ between inflow and turbine heading, McNaughton [34] showed using CFD simulations that C_P remains constant, such that power from the turbine is then given by equation (8).

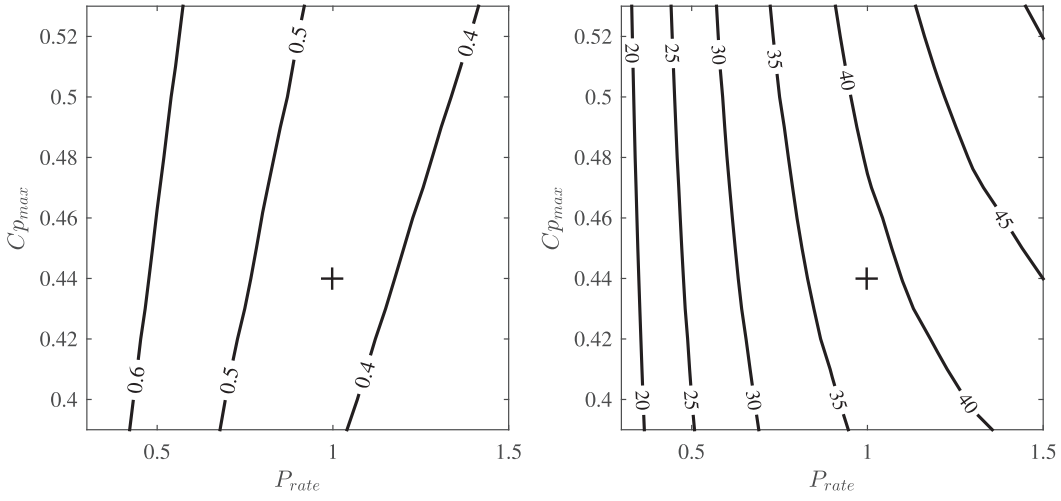

(a) Capacity factor

(b) Annual yield, GWh

Fig. 6. Contours of capacity factor (a) and annual energy yield (b) for X = 10 D_t stream-wise and Y = 1.5 D_t cross-stream spacing. Chosen turbine specification (+).

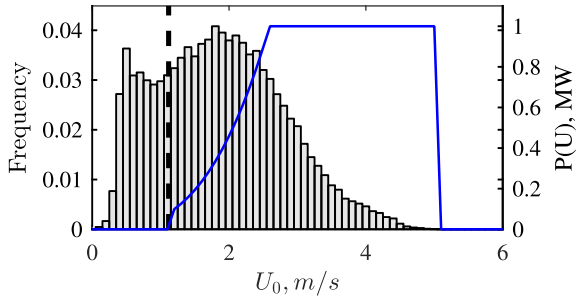

Fig. 7. Histogram showing current speed probability distribution with the turbine's 1 MW power curve (blue) and cut-in speed (dashed). (For interpretation of the references to colour in this figure legend, the reader is referred to the web version of this article.)

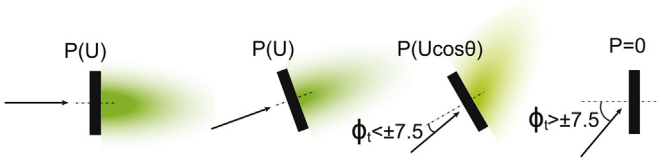

Fig. 8. Implementation of a Slack-tide yaw control strategy.

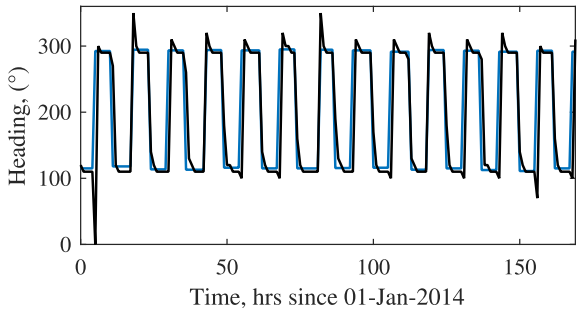

Fig. 9. Variation of turbine heading (blue) and current heading (black). (For interpretation of the references to colour in this figure legend, the reader is referred to the web version of this article.)

$$P = \frac{1}{2} C_P \rho A (U_0 cos\phi_t)^3 \quad (8)$$

For misalignment angles greater than ±7.5°, the turbine power output is assumed zero. Implementation of the slack-tide strategy in the model is schematically represented in Fig. 8, with the corresponding variation of turbine heading shown for a seven day period in Fig. 9

Based on the tidal resource during the full year 2013, slack-tide yaw increases yield by ≈5% above a fixed mechanism (Table 1). This is because the site has a single distinct ebb and flood direction separated almost exactly by 180° (Fig. 10). In contrast, the whole three and a half year period exhibits significant directional variation (Fig. 10). Over the full period, the continuous yaw mechanism captures the most energy but a slack-tide yaw strategy yields 90% of this and also yields 2.6 times more energy than the fixed strategy, with a capacity factor of 0.394 compared to just 0.153. Hence a slack-tide yaw strategy has been selected for the remaining analysis.

3.4. Wave operating conditions

Tidal turbines are expected to have a shut-down criteria based on significant wave height, H_s [35] in order to protect the turbine from extreme wave loads. Wave buoy data of significant wave height, H_s, peak wave period, T_p and corresponding direction, θ_p have been used for the six month interval, 17 Jan 2012–17 Jul 2012. The buoy is located at 3.2792°W, 58.6750°N, approximately 8 km West of the case-study site centre and is one of the longest continuous datasets available near to the array. The buoy data, stored at 30-min intervals, is time-averaged to an hourly interval to coincide with that of the tidal and wind resource data.

The wave shut-down criteria has only been applied to this seven month interval of the wave dataset. Future work will investigate correlating the buoy data to numerical predictions of wave conditions such as from ERA-Interim. The sensitivity of energy yield based on a range of H_s shut-down thresholds is shown in Fig. 11. Limiting the operating range to $H_s < 2.5$ m reduces energy yield by 5%, although it is noted that this time interval neglects the months October–December where the occurrence of wave conditions exceeding $H_s = 2.5$ mare expected to be more frequent, and so is likely to be an under-estimate of the impact on energy yield. Similarly the increase in yield offered by operating a higher shut-down criteria will be more significant for more exposed sites.

4. Steady-state load modelling

The environmental loads acting on an offshore support structure considered here are due to wind, wave and current. Design codes are available for assessment of turbulent wind loading and wave loading on offshore wind support structures [36]. The first such code for tidal turbine loading was released in DNV GL [37], with various simplified approaches available for consideration of tidal turbine loads due to turbulent flow and waves. Complete design requires consideration of dynamic loads. However, initially, it is informative to determine the range and occurrence of steady-state loads to assess how the loading of a structure within a co-located system may differ to the loading of structures supporting individual wind or tidal turbines. This is useful to identify the position within a tidal array where it would be most suitable to co-locate a wind turbine. Extreme loads are also of interest as these govern support structure sizing for survivability. Here, extreme loads are considered as a combination of those defined in DNV-OS-J101 [36] for offshore wind turbines and the severe operational cases defined for tidal turbines in DNV GL [37].

The maximum still water level (SWL) of the Inner Sound is 35 m [38], which is beyond the limits seen for traditional monopiles. Instead, a braced monopile support structure (tripod) has been

Table 1
Energy yield (GWh) and capacity factor (CF) for the periods 01 Jan 2012–01 May 2015 and 01 Jan 2013–31 Dec 2013 from a small array of 2 rows of 5, 1 MW turbines in a rectilinear arrangement with 1.5 D_t lateral spacing and 10 D_t longitudinal spacing.

		Fixed	Slack-tide	Continuous
2013	Energy	20.24	21.23	33.95
	CF	0.231	0.242	0.388
2012-15	Energy	44.7	115.0	127.7
	CF	0.153	0.394	0.438

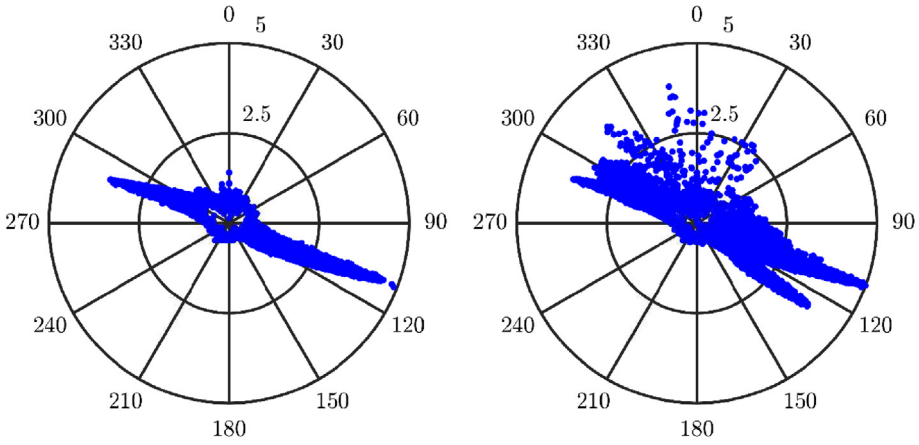

Fig. 10. Tidal roses of current speed and direction at site.

analysed (Fig. 12). Dimensions are the same for each individual system, except that the tidal turbine support structure extends from the bed to hub-height (17.5 m) only, whereas the structure supporting both a wind and tidal turbine extends through the mean water line. For the wind-only system there is no tidal turbine. The centre column of the support structure was defined as 3.5 m diameter, typical for a 3.6 MW wind turbine [39], with braces up to a height, $H = (SWL - D)/2$ from the sea-bed. A 1/7th power law [40] was used for both the current and wind shear profiles in order to extrapolate from hub height to the sea-bed and free-surface, respectively, although these can be defined independently.

4.1. Wind loading

Thrust loading due to wind turbine operation is obtained using the same thrust curve as used in the energy yield calculation, see Section 2. The part of tower above water line is considered in two regions (see Fig. 12). An upper section behind the swept area of the wind turbine rotor (shaded) and a lower section below the rotor and down to the still water level (SWL). Each section is divided into 1 m segments. The drag coefficient, $C_{D,w}$ for the top of each segment height is calculated using Reynolds numbers, R_e for a circular cylinder as specified in BSI [41] and subsequently the maximum drag force, F_w is obtained for each segment as equation (9).

$$F_w(z) = \frac{1}{2} C_{D,w}(R_e) \rho A U_w(z)^2 \tag{9}$$

where density, $\rho = 1.225$ kg/m^3 for each segment frontal area, A and $U_w(z)$ is the turbulent wind speed at height z, the treatment of which is described below.

Equivalent net force on the whole tower is obtained as the summation of each segment force with the moment arm obtained through summation of moments about the tower base at the sea-bed. During shut-down, drag on each of the three blades is defined by $C_D = 1.3$ and the projected area as defined in DS 472 1992 [42].

For the treatment of turbulence, a Reynolds decomposition into a steady mean, $\overline{U}_w$ and fluctuating term, U'_w, eqn. (10) can be substituted:

$$U_w = \overline{U}_w + U'_w \tag{10}$$

where U_w is the wind velocity.

The turbulence intensity, I is defined at hub-height as:

$$I = \frac{\sigma}{\overline{U}_{hub}} \tag{11}$$

where σ is the standard deviation of the stream-wise component of hub-height wind speed, U_{hub}.

Due to the numerical wind resource data only being an hourly average, there is no information regarding turbulence intensity at the site. Where such information is lacking, the standards [43,44] define different profiles for the 90th percentile of the distribution of standard deviation of wind speed, σ_{90}. In this study, the definition of the Normal Turbulence Model (NTM) from DNV [36] for normal operating conditions is used:

$$\sigma_{90} = I_{15}(0.75U_{hub} + b); b = 5.6 \text{ m/s} \tag{12}$$

where I_{15} is a reference turbulence intensity defined at 15 m/s. For onshore wind turbine classes A-C, I_{15} varies between 12 and 16%. For offshore wind turbines, no such classes exist and so a more appropriate reference intensity is required. Turk and Emeis [45] and Westerhellweg et al. [46] provide turbulence intensities at

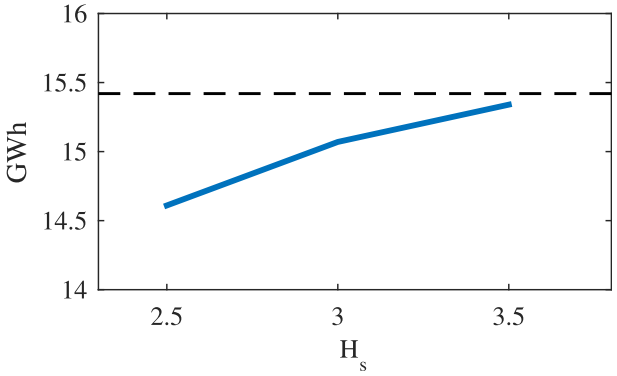

Fig. 11. Energy yield (blue) for the period 01 Jan 2012–01 May 2014 from a small array of 2 rows of 5, 1 MW turbines in an aligned arrangement with 1.5 D_t lateral and 10 D_t longitudinal spacings, for a range of H_s shut-down thresholds. Limit of no constraint on H_s (dashed). (For interpretation of the references to colour in this figure legend, the reader is referred to the web version of this article.)

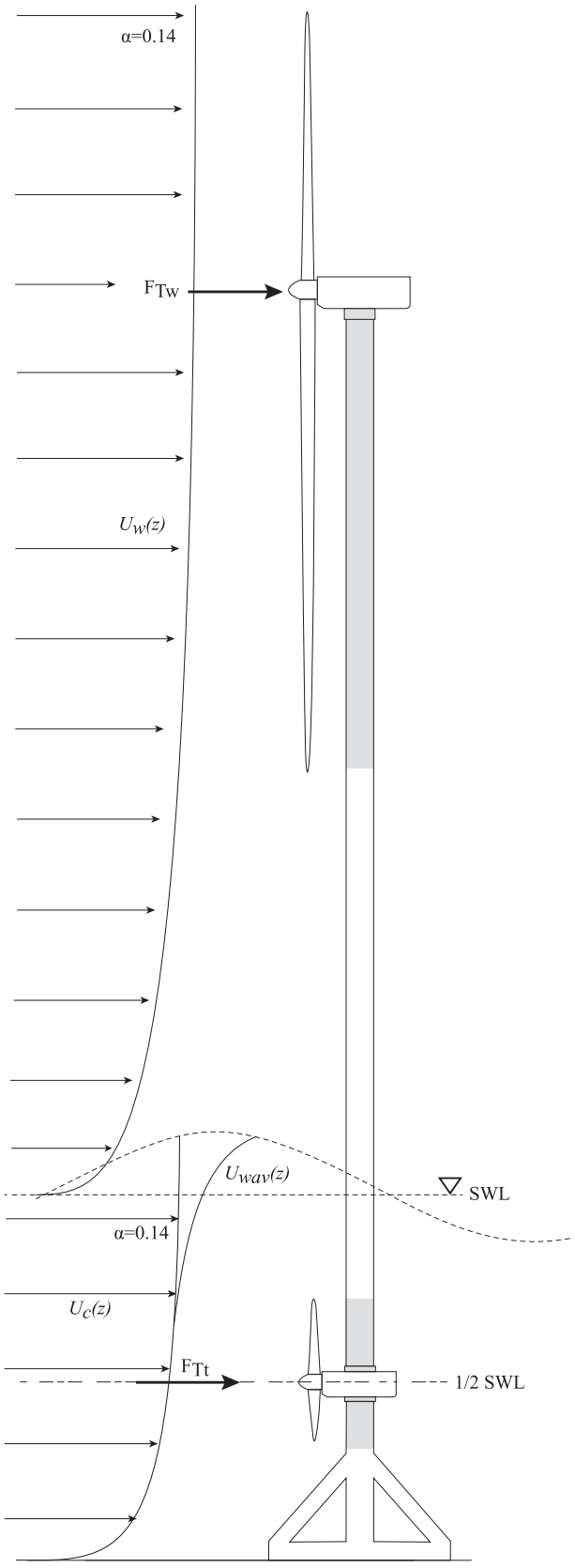

Fig. 12. Sketch of arrangement of combined system showing treatment of environmental loads. Grey sections indicate parts of the structure which are only considered for loading during turbine shut-down. The wind-only structure is the same as depicted here, except without a tidal turbine mounted, while the tidal-only structure has no support above its nacelle.

around 100 m height for the FINO 1–3 measurement stations in the North Sea typically of between 4.5 and 7% at 15 m/s. However, these sites are far from shore (FINO 1 is 45 km from shore) whereas the nearest wind turbine in this study is only 500 m from shore. The proximity to shore is not expected to have a great impact on turbulence intensity though, since based on the definitions of site complexity given in BSI [47] the maximum elevation of land within 1.8 km (20 hub-heights) of the nearest turbine is only around 40 m, and so the site is not considered complex. However, a reference value from a site closer to shore is desired. Hansen and Larsen [48] give the turbulence intensities for coastal sites, Nasudden and Skipheia as approximately 6% for heights around to 100 m. This is similar to that seen for the FINO stations which contradicts the fact that turbulence intensity typically decays with distance from shore. An alternative approach is to consider the expected mean standard deviation of the 10-min averaged wind speed, U_{10} given in DNV [43]:

$$E[\sigma] = U_{10} A_x \kappa \frac{1}{ln(z/z_0)} \tag{13}$$

where $A_x = \sqrt{4.5 - 0.856 ln(z_0)}$ and can be considered as 2.4 for flat terrain with z_0 coming from the implicit Charnock relation:

$$z_0 = \frac{A_c}{g}\left[\frac{\kappa U_{hub}}{ln(z_{hub}/z_0)}\right]^2 \tag{14}$$

where $\kappa = 0.4$ is the von Karman constant and $A_c = 0.034$ for near-coastal locations.

Assuming the standard deviation of the 60-min average wind speed to be independent of that for U_{10}, this same definition then provides $I_{15} = 8.7\%$. Although this is higher than the 6.5% seen for the above offshore sites, it is lower than the 12% considered by the onshore standards and so seems a suitable reference intensity to use without further site-specific information.

As such, the fluctuating wind speed is defined in the model as:

$$U'_w = \pm I_{90} \overline{U}_w \tag{15}$$

where $I_{90} = \sigma_{90}/\overline{U}_w$.

The impact of wake effects on turbulence are not considered in this study since peak loads are expected to occur on the front row of turbines in a dominant wind heading which is not affected by the wakes of upstream turbines.

4.2. Support structure loading in turbulent current and waves

Loading on fixed slender structures due to waves and current is typically approximated by a Morison type drag and inertia formula:

$$F = \frac{1}{2} C_D \rho A U(z)^2 + \rho V C_m \dot{U}(z) \tag{16}$$

where z is the depth variation below the wave surface, η; and C_d and C_m are coefficients of drag and inertia, respectively.

In the case of combined waves and current, the velocity components of each, normal to the cylinder, N, are vectorially summed first, to give:

$$F_N = \frac{1}{2} C_D \rho A U_N |U_N| + \rho V C_m \dot{U}_{wav} \cos\phi_{wav} \tag{17}$$

where A is the projected area, V section volume, $\dot{U}_{wav}$ the wave-induced particle acceleration and subscript N has been introduced to indicate the component normal to each structural member, such that:

$$U_N = U_c \cos\phi_c + U_{wav} \cos\phi_{wav} \quad (18)$$

with subscripts c and wav corresponding to current and wave-induced velocities, U and directions, ϕ relative to structure orientation, respectively.

In the case of very small waves the drag force is only due to current. Here, the drag coefficient, C_D is defined as a function of Reynold's number, R_e for a rough cylinder of specified roughness coefficient (1×10^{-2}) [43]. In the case of waves, the flow around the support is always assumed to be post-critical $(R_e > 10^6)$ since for waves of most practical interest, R_e remains post-critical [43]. The KC number is modified to include the in-line current velocity:

$$KC = \frac{(U_{wav} + U_c)T_P}{D} \quad (19)$$

such that as U_c is large, the drag coefficient tends to its steady-value, $C_{D,S} = 1.05$. For $U_c > 0.4U_{wav}$ and all non-vertical cylinders of the braced section of the structure, the steady-value $C_{D,S}$ is also assumed. The inertia coefficient, C_m, is defined as a function of KC according to [49].

In the case of turbulent current, a analogous treatment to that defined for the wind turbines is used, starting with a Reynolds decomposition into a steady mean, $\overline{U_c}$ and fluctuating term, U_c':

$$U_c = \overline{U_c} + U_c' \quad (20)$$

where U_c is the current velocity.

Turbulence intensity is known to vary with location, with current speed and depth in the water column. Here a depth-averaged value of 10% is used. This is lower than the values 17% and 13% observed by Hardwick [29] for ebb and flood respectively in the Inner Sound of the Pentland Firth but consistent with analysis of [51] who observed 8–10% turbulence intensity at the Falls of Warness and in-line with studies at other sites [52,53]. Drawing from the wind standards Normal Turbulence Model (NTM) [36] it was shown in the treatment of wind turbulence, a characteristic standard deviation can be defined as the 90th percentile of the distribution of standard deviation. Assuming the current turbulence is normally distributed about the mean, this would be $1.28\sigma_c$. This was the approach used by Thomson et al. [53] who also notes that further research is required to assess its suitability. In contrast, the NTM actually defines a specific variation of σ_c relative to wind speed (see equation (12)). Simeón and Ferreira [54] assessed the suitability of such a distribution applied to current speeds in the Falls of Warness and found that the definition works well for the flood tide and although it doesn't predict the ebb turbulence intensity well, the agreement is within $(1.28 \pm 1\%)\sigma_c$ and so is a suitable definition without further information available. As such, the fluctuating current speed is defined in the model as:

$$U_c' = \pm 1.28 I \overline{U}_c \quad (21)$$

This expression characterises the turbulent intensity of the ambient flow only and neglects turbine generated wakes and elevated kinetic energy due to wave induced kinematics. For the array considered, streamwise spacing is 20 D_t and so turbulence due to upstream turbines is considered to have decayed to the ambient level (turbulence decays faster than velocity deficit). However, for arrays with significantly smaller streamwise spacing the effect of wake-generated turbulence should be considered. The fluctuating kinetic energy of linear waves propagating over a turbulent channel can be treated as a superposition of current-only TKE and kinetic energy associated with the amplitude of wave-induced kinematics [55]. As such, the presence of waves is assumed to have negligible affect on the turbulence intensity of the site and wave-induced loads are treated separately as described below.

The wave kinematics, U_{wav} and $\dot{U}_{wav}$ are predicted as a function of depth and wave phase, ψ, using the SAWW model [56] for a range of H_s and T_p combinations. SAWW is a non-linear wave model based on a 20-term Fourier series numerical approximation method for steady water waves [57] with initial conditions defined by linear wave theory and solved for using Newton-Raphson iteration. The water particle velocities and accelerations are output for 35 section heights, linearly spaced between sea-bed and wave elevation at phase intervals of $\pi/20$ radians. For very small values of H_s and T_p the wave motion is assumed to tend towards a current-only condition. The current velocities are obtained at each support structure from the tidal wake model velocity field and extrapolated from hub-height along the shear profile. This profile is stretched from the SWL to wave surface, η using the non-linear

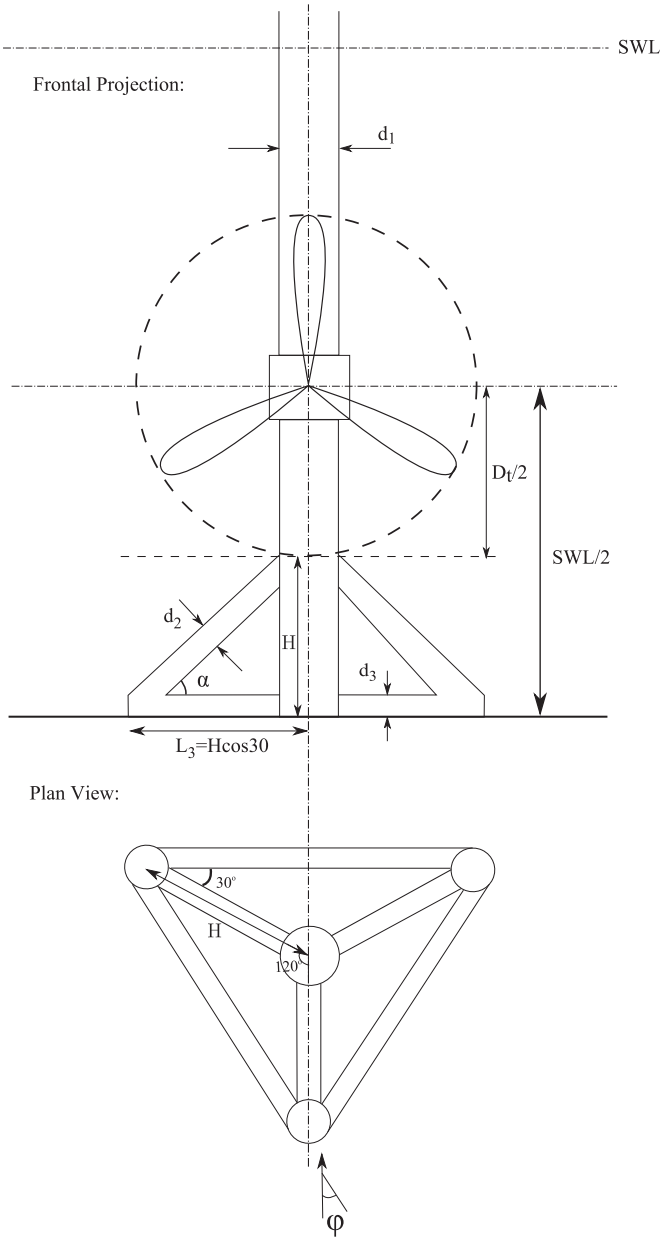

Fig. 13. Detailed dimensions of braced section of support structure. Dimensions are quantified in Table 2.

Table 2
Dimensions of braced structure, with reference to Fig. 13.

	Dimension
SWL	35 m
H	$SWL/2 - D_t/2$
d_1	3.5 m
d_2	$d_1/3$ m
d_3	$d_1/7$ m
α	$\tan^{-1}(H/L_3)^\circ$
ϕ	$[0, 30, 60]^\circ$

stretching method defined in DNV [43].

Dimensions for the braced section are shown in Fig. 13 and provided in Table 2. These were sized according to a simple space-truss analysis of buckling load, with wall thickness to section diameter ratio set to minimise material volume.

Loading on the immersed part of the structure is considered in three sections (see Fig. 12); area above the tidal rotor (upper), area behind the rotor swept area (mid) and the braced section area below the turbine rotor (lower). The force normal to each member of the braced structure is calculated using the component of combined wave-current velocity normal to the member [43]. Shielding effects of members in the braced section are ignored. During turbine operation, drag due to the section of tower behind the rotor swept area is ignored. The reduction in water level seen across the rotor is not accounted for, nor is the corresponding increase in velocity seen in the bypass flow around the rotor. The change in depth with the tide is also neglected. Forces are calculated for 30° direction sectors to account for the orientation of the structure relative to the wave direction.

The peak overturning moment, M_{max} caused by a wave occurs at the corresponding peak-phase, ψ_{max} (eqn. (22)). There is a subtle difference between the phase corresponding to maximum overturning moment as opposed to maximum force. Fig. 14 shows the difference in phase between the normalised net force and moment variations for wave-current loading. Both curves are for $H_s = 2.5$ m and $T_p = 10.5$ s, found to be representative of the maximum load scenario 3 in Table 4 (see Section 6.2). For the full range of H_s and T_p considered, the maximum shift in phase was less than $\pi/10$ radians.

$$M_{max} = \max\left\{ \sum_{z=0}^{\eta} F_{wav}(z,\psi) h(z,\psi) \right\} \tag{22}$$

For breaking waves, [58] shows that the wave force can be 2.8 times greater than the total force predicted by using SAWW. The breaking wave height is defined by the Miche criterion, as:

$$H = 0.142\lambda \tanh(kd) \tag{23}$$

where $k = 2\pi/\lambda$ is the wave number.

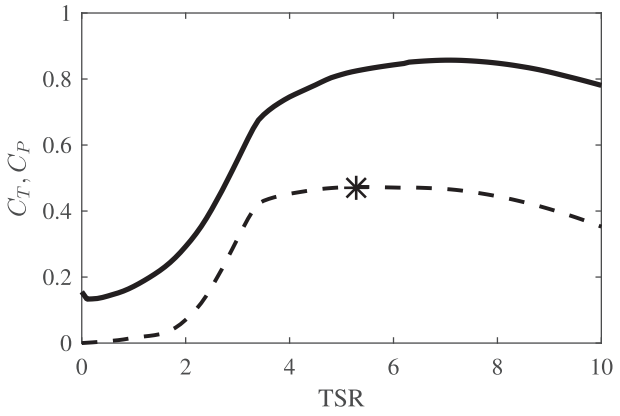

Fig. 15. Coefficients of thrust, C_T (solid) and performance, C_P (dashed) vs. tip-speed ratio (TSR) for the full-scale, fixed pitch turbine. Maximum C_P (*).

For waves which exceed the Miche criterion, the total wave force, $\sum F_{wav}(z)$ is corrected by the *kd*-force correction profile suggested in Stansby et al. [58] and the difference is applied at the wave crest elevation to assume a worst-case overturning moment. In the splash zone, the wind drag force and wave force are both included.

A large look-up matrix as a function of all resource variables is then generated. This is used in conjunction with the hourly time-series of resource data, as used in Section 3, to obtain a quasi-steady time-series of force variation with height. Since the peak loads acting on the structure are of interest, at each time step of H_s, a deep water approximation is assumed [59], whereby the range of wave heights are then governed by a Rayleigh distribution eqn. (24).

$$f(H) = \frac{H}{\sigma^2} \exp\left\{ -\left(\frac{H}{\sigma\sqrt{2}}\right)^2 \right\} \tag{24}$$

where σ_H is the standard deviation of wave height.

The 1% exceedance height, $H_{1/100}$ (25) is then used to linearly interpolate to from the look-up matrix and obtain the corresponding peak force distribution.

$$H_{1/100} = H_s \sqrt{\frac{1}{2} ln(100)} \tag{25}$$

which gives $H_{1/100} = 1.52 H_s$.

4.2.1. Rotor wave and current loading

As applied for the energy yield model, the turbine is assumed to shut-down for $H_s > 3$ m. However, for $H_s < 3$ m, the turbine will be operating and hence be subject to oscillatory wave-current loading.

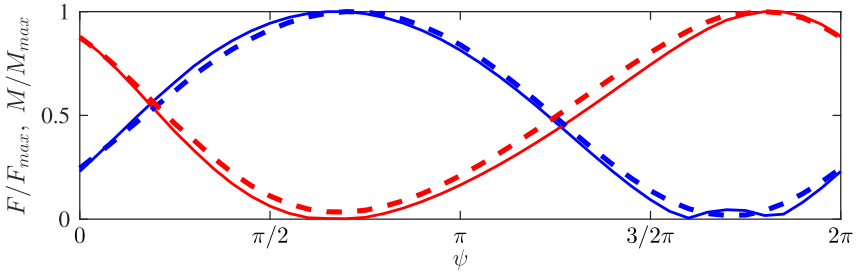

Fig. 14. Phase-variation of normalised magnitudes of net force (dashed lines) and over-turning moment (solid lines) for $H_s = 2.5$ m, $T_p = 10.5$ s with in-line (blue) and opposing (red) current of speed $|U_c| = 2.5$ m/s. (For interpretation of the references to colour in this figure legend, the reader is referred to the web version of this article.)

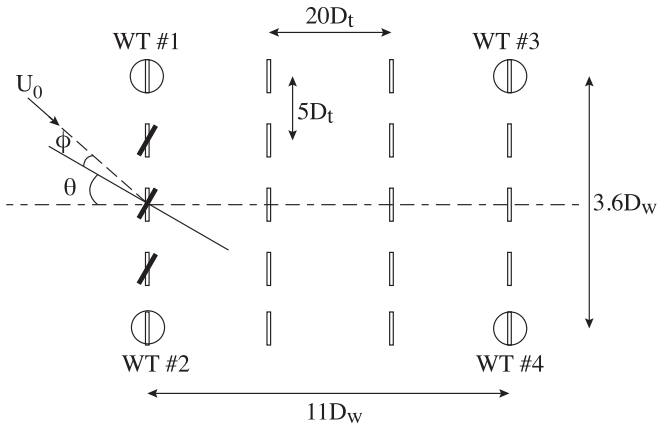

Fig. 16. Farm footprint of 12 MW wind capacity co-located with 20 MW tidal capacity, showing footprint heading (horizontal dashed line), angle of yawed turbines (▬) relative to footprint heading, θ, angle ϕ of onset flow, U_0 relative to the yawed turbine's axis and relative spacing of wind turbines (◦) and tidal turbines (▭). Not to scale.

The rotor force due to combined waves in a turbulent current can be established by separately decomposing the drag force components of the Morison equation into a drag force due to steady current loading, $F_{T_{tide}}$ and a drag force due to oscillatory wave loading, $F_{wav,rot}$ [60]. The steady-current drag force is obtained using a full-scale thrust curve for a fixed-pitch turbine (Fig. 15).

For misalignment, ϕ of the steady-current to the turbine axis, the thrust force is calculated as eqn. (26):

$$F_{T_{tide}} = \frac{1}{2} C_T \rho A U_c \cos\phi |U_c \cos\phi| \tag{26}$$

The wave drag force in-line with the rotor is then given as:

$$F_{wav,rot} = \frac{1}{2} \rho A C'_D U_{wav,rot} (U_c \cos\phi + U_{wav,rot}) \tag{27}$$

where $C'_D = 2$ is the average oscillatory drag coefficient obtained from Fernandez-Rodriguez [61] for $KC > 0.25$ and $U_{wav,rot}$ is the component of the wave-induced velocity acting in the turbine's rotor plane and averaged over the rotor area (as in eqn. (7)) and applied at hub-height.

During shutdown, drag of the three blades is considered for current-only loading and is accounted for in the same manner defined for the wind turbine in Section 4.1.

5. Energy yield assessment

A farm of 4 rows of 5 No. 1 MW tidal turbines co-located with 4 No. 3 MW wind turbines are considered at a site with an approximate area of 1100 × 360 m within the Inner Sound of the Pentland Firth. The farm footprint is given in Fig. 16 with the relative turbine spacings.

Table 3 presents energy yield for the 3.5 year period, excluding December 2012. The addition of 12 MW wind capacity to the 20 MW tidal array increases the net energy yield by over 70%. Based on idealised energy yield for each system, wake losses of 9% and 6.5% are calculated for the tidal and wind-only systems respectively. The capacity factors are also shown, with the combined farm being a weighted-average of the two isolated systems, weighted by the capacity of each system relative to the aggregate capacity. It is noted that the wind farm capacity factor is quite high and greater than the 35% average typically seen for offshore wind farms [30]. This occurs because the wind turbines are under-sized for the given wind resource. However, a larger rated capacity wind turbine would require larger spacing, particularly on the cross-stream spacing which is already small at just $3.6D_w$. This would also mean fewer wind turbines for the same number of tidal turbines which would reduce the improvements seen in co-located energy yield and may also reduce the impetus for using shared support structures, since despite the expected cost savings, there would be fewer number of 'standardised' shared structures and this would limit the potential for cost reduction.

Table 3
Energy yield for the period 01 Jan 2012–01 May 2015 (excl. Dec 2012) from a farm of 4 No. 3 MW wind turbines arranged regularly with $11D_w$ longitudinal and $3.6D_w$ lateral spacing co-located with 4 rows of 5, 1 MW tidal stream turbines in an aligned arrangement with 5 D_t lateral and 20 D_t longitudinal spacings. Idealised energy yield for no wakes is shown in brackets.

	Tidal-only	Wind-only	Combined
Energy, GWh	242.4 (273.6)	181.7 (194.4)	424.1
Capacity factor (CF)	0.426	0.533	0.466

The time-varying power for each system in isolation versus the combined system power output is shown for the period 01 Jan 2013 to 31 Dec 2013 in Fig. 17 a). Previously, the diurnal power variation from a co-located farm was studied in Sudall et al. [28], showing differences in combined power output for neap and spring tides during summer and winter. It was found that during neap tides the combined power supply could be entirely dependent on the wind-only, which during summer months might be significantly lower than during winter months when the average wind speed is higher. Conversely, during a spring tide, the co-located power output would feature a regular supply from the tidal turbines, with the magnitude of the peak output varying as the wind. This same trend is demonstrated in the 28-day period considered in Fig. 17 b), where the combined supply has a regular fluctuation governed by the tidal variation, but during the neap tide around 22nd January, the combined supply is almost entirely wind dependent.

The multi-year interval considered allows analysis of the monthly-moving average and year-to-year variation of power output as in Fig. 17 c). The tidal variation is almost constant across the years 2013 and 2014. The final 3.5 months (01 Jan 2015–15 Apr 2015) features a significant drop in tidal power and similarly, the first quarter of 2012 also has reduced power output, which is reflected in the reduced average power output seen for these periods. For this period of 2012, there is actually a shift in the tidal heading from being centred approximately around 303° N during the flood tides prior to 28 Mar 2012, to being centred around 293° thereafter. This means during power generation, the turbines would be yawed relative to the array footprint heading (set at 293° to maximise annual energy yield) and so produce less power. For the period 01 Jan 2015 onwards, this reduced power is also due to a change in the direction of the tide, but during each flood tide. From 03 Feb 2015 the flood tide heading starts varying by approximately ±15° compared to varying by approximately ±4° before this date. The ebb tide appears to be unaffected. There is limited published data available concerning historical changes to the FOAM model and so the cause of these direction changes remains a topic for further investigation. However, the effect is that the flow is misaligned with the turbine heading more frequently during each flood tide, for which the turbines cannot generate any power outside of inflow headings of ±7.5° and hence the reduced average power. The annual average wind power is almost identical for each of the three complete calendar years. It is noted that the average power output is higher during the final four months' of data, due to the higher wind speeds which occur over the winter months. For each year, the wind exhibits reduced power output during summer,

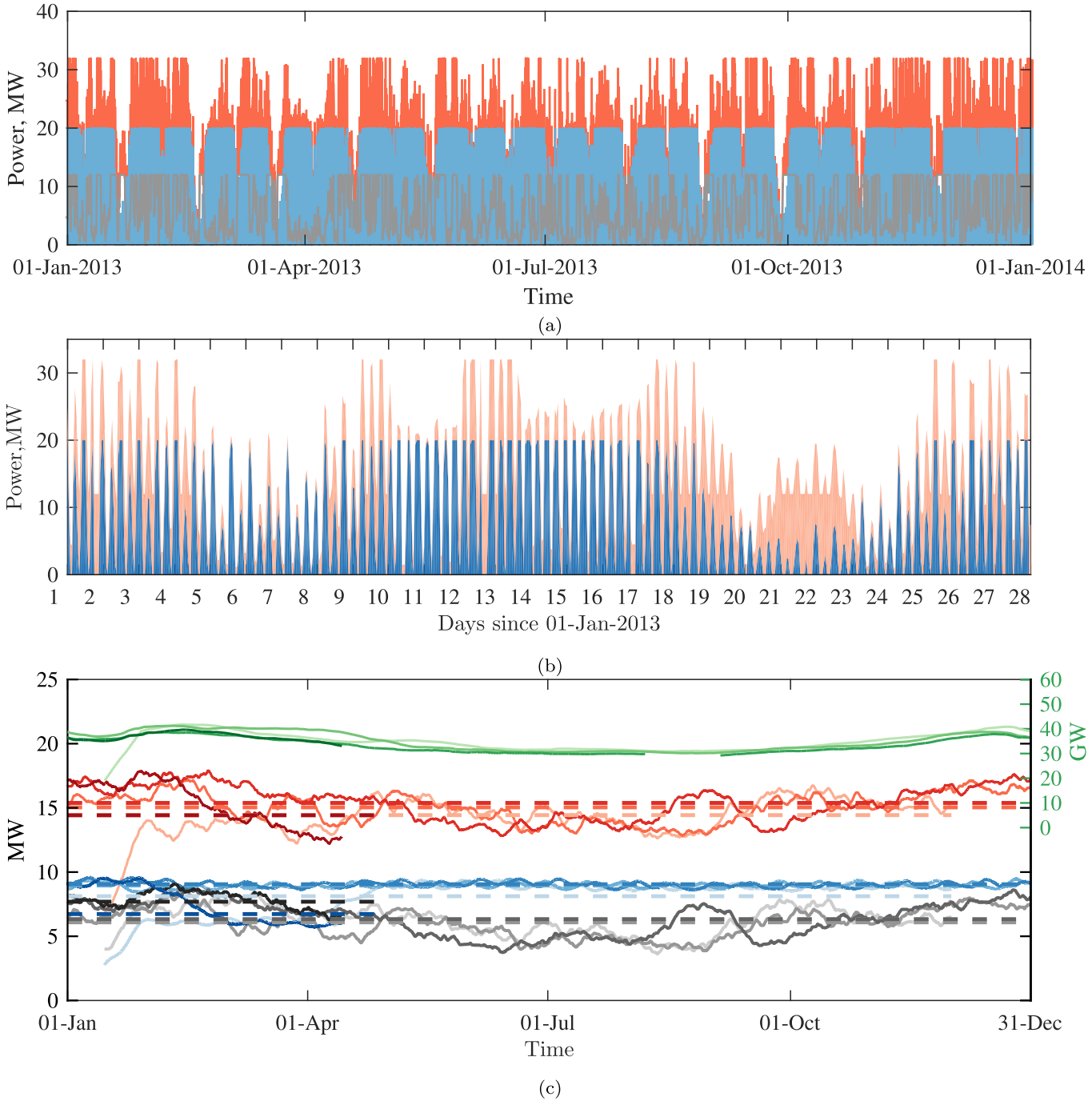

Fig. 17. (a) Power-time variation in MW for wind-only (grey), tidal-only (blue) and combined (red) for the 12 month period, 01 Jan 2013 to 31 Dec 2013; (b) the contribution to total power from wind (pale-red) and tidal (blue); (c) monthly moving-averages of wind (grey-scale), tidal (blues) and combined (reds) power variation in MW versus UK electricity demand (greens) in GW for the years 2012–2015 stacked in order of increasing colour intensity. Annual averages for each year are also shown (dashed lines). Note: data for 2012 begins 15th Jan so the moving average is not skewed by zero data; similarly, data for 2015 ends on 15th Apr. (For interpretation of the references to colour in this figure legend, the reader is referred to the web version of this article.)

increasing over autumn to give peak output through December and January. This trend is also translated onto the combined power output, and is coherent with the tidal power monthly-moving average variation being almost constant. This is a convenient result if significant up-scaling of co-located deployment was considered, since this is also the trend seen in the annual UK electricity demand (green).

The variability of power and in particular, the rate of change of power is an important factor for the power network, since the network frequency needs to be maintained within a given tolerance. It therefore gives an indication of the level of storage capacity or reactive power required in the network. The standard deviation of each system normalised by the system's respective capacity allows comparison of the distribution of power about the mean for

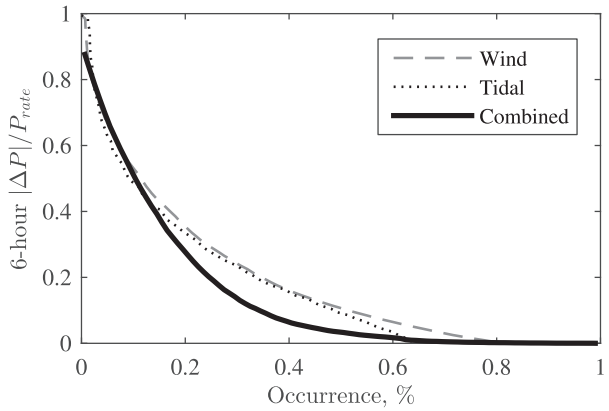

Fig. 18. The absolute change in power every 6 hours normalised by the capacity of each system versus the percentage of occurrence.

systems of differing capacities. In this study, these normalised standard deviations are 0.36, 0.40 and 0.28 for wind-only, tidal-only and the combined systems respectively. This shows that a combined system has 22% smaller standard deviation than a wind farm of the same capacity. The result is slightly surprising for the tidal-only system since the tides are predictable and hence are expected to be less variable than for wind. However, with the tidal current principally governed by the semi-diurnal lunar constituent, M2 the tide changes from slack to peak ebb or flood every 6.21 hours, resulting in a corresponding change from zero to rated power output over the same period. Since the tides are well predicted by their harmonic constituents, it is logical to look at the change in power over this period as this would represent how much of the change in power is difficult to predict. Although short-term forecast methods can also predict wind speeds fairly reliably for up to 6 hours in advance [62], observing the change in power over 6-hour intervals accounts for changes in power which are expected to occur, without any detailed prediction methods being available. The rate of change of power, the so-called 'ramp rate', is shown in Fig. 18 and although the tidal-only system shows a smaller ramp rate compared to the wind-only system, the combined system has the smallest rate of change. For example, for less than 20% of the time the change in power of the combined system is greater than 27% of capacity, whereas the corresponding change for the wind and tidal-only systems would be 36% and 33% respectively.

6. Support structure load variation

This section presents the results of the environmental load modelling for each of the three support structure types considered: wind-only, tidal-only and combined. The force variation with height of the structure is obtained, however the focus here is on the overturning moment these generate about the base of the structure since this indicates the overall strength required and subsequently structural dimensions and material usage.

6.1. Load time-series

The time-history of overturning moment for the tidal-only, wind-only and combined systems over the six months studied, is shown in Fig. 19 along with the variation of wind, tidal and wave-induced velocities. Peak wind-only bending moment is 95.3 MNm (21 Jan 2012), whereas peak tidal-only bending moment is almost 60% lower, at 39.5 MNm (10 Mar 2012). The latter occurs during a spring ebb tide with $H_s = 2.95$ m, prior to the wave shutdown of the turbine, and at a wave heading within 20° of the current heading (see ● marker in Fig. 19). The combined system peak overturning moment is 98.4 MNm occurring on 05 May 2012, the same time as the second-greatest wind-only overturning moment. The dominance of wind loads relative to tidal loads is consistent with our earlier findings [28] although the tidal loads are greater here due to the different tidal resource model. In this study, wave loads are also considered and the trend still holds with peak overturning moment for the combined structure 3% greater than the peak wind-only overturning moment.

6.2. Extreme load scenarios

Four operational load scenarios are considered for the co-located structure in Table 4. These scenarios are selected as they represent different combinations of wind- and tidal-turbines operating close to rated power and shutdown respectively. These effectively represent the 'severe operation' conditions defined in [40] and [37] for wind and tidal turbines respectively. A fifth case for both turbines shutdown is also considered where the tidal turbine is shutdown due to the H_s shutdown criterion rather than the shutdown speed criterion. For each shut-down criterion, 'max' and 'min' refer to the largest and smallest value of the peak load predicted to occur during each 1-hour combination of environmental conditions.

The vertical variation of force for each of the five load cases of Table 4 is also shown in Fig. 20. Most notable from these curves is that the magnitude of force on the submerged section of the structure is of a similar order of magnitude to the thrust force on the wind turbine. However, due to the greater moment arm of the wind turbine thrust, the submerged loads do not contribute significantly to the net overturning moment. The difference in height of the submerged loads between the shutdown-shutdown (case 5) and rated-shutdown (case 2) cases gives an indication of the resulting splash zone.

Finally, it should be noted that the magnitude of force increases significantly at the base of the structure, this is due to the horizontal cross-bracing at the bottom of the structure which presents a relatively large projected area to the flow. However, since these are located within the bottom metre of the structure, these do not contribute greatly to the overturning moment.

For the tidal-only array, the variation of mean moments with turbine position within the array are considered in Fig. 21. Turbines at locations 1–5 have the greatest mean loads due to the heading of the dominant flood tidal current. Turbines on the northern edge of the array also have greater mean loads than those on the southern edge of the array due to more occurrences of misalignment of the flood tide occurring to the north of the footprint heading rather than to the south. The turbine with lowest mean load is at location 15, for which the load is less than for turbines on the eastern edge of the array during an ebb tide due to shadowing. The difference in mean loads for the maximum loaded turbine, location 1 and the least loaded, location 15 is 0.54 MNm or 6.3% of the load seen by the turbine at location 1. The force probability distributions for these two turbines are shown in Fig. 22 along with their corresponding 98th percentile loads which give an indication of the peak loads with a 50 year return period. The 98th percentile loads vary as 28.39 MNm and 27.91 MNm for turbines at locations 1 and 15 respectively, a difference of 1.7%. Given that this maximum 98th

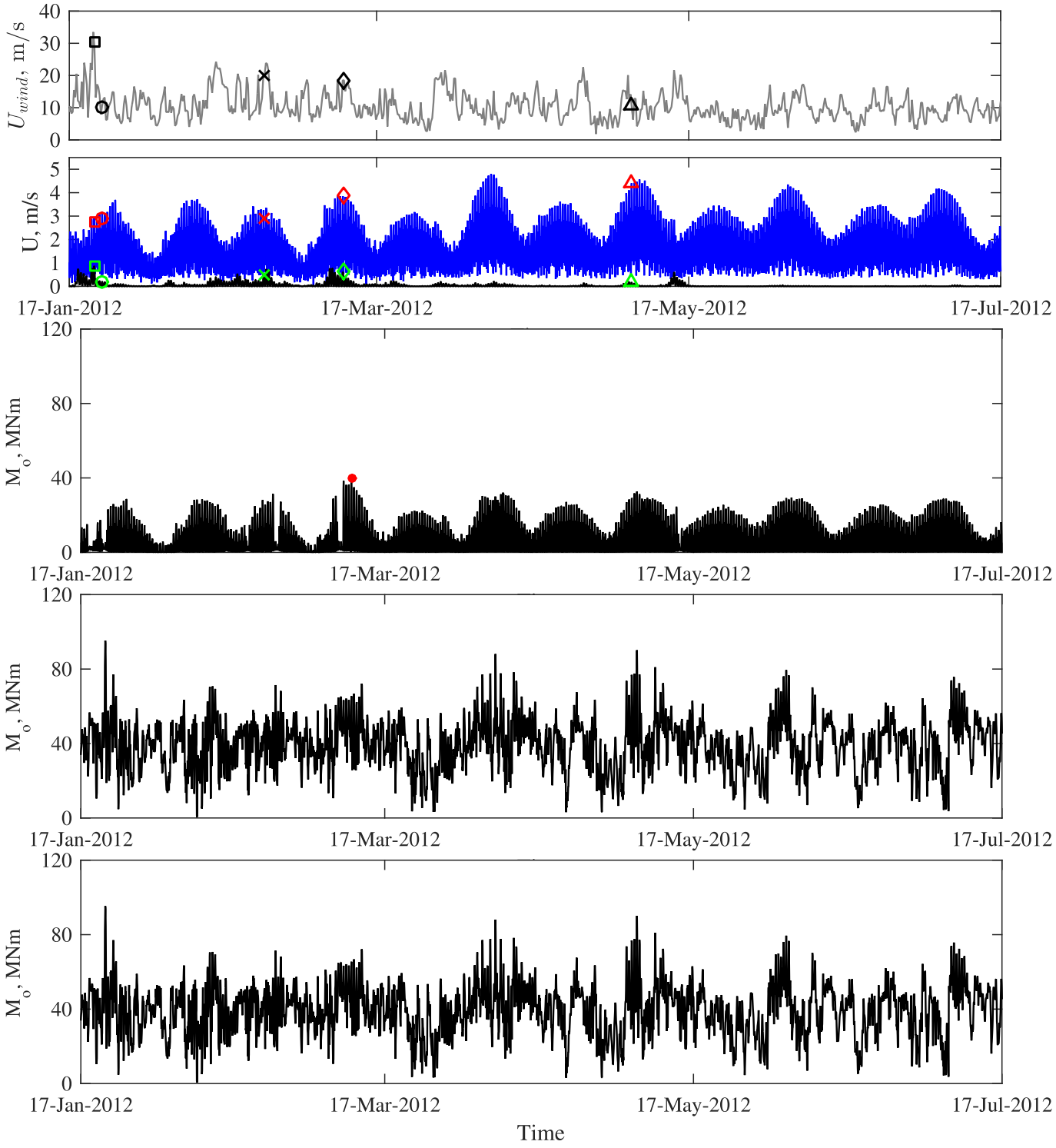

Fig. 19. From top (a) to bottom (e): hourly, time-histories of (a) Wind speed; (b) Current speed (blue) and wave-induced velocity (black); with base bending moment for (c) combined, (d) tidal-only and (e) wind-only, all at turbine location 1 (see Fig. 16), which experiences the greatest mean overturning moment during the 6-month period of coherent wind, wave and current data. The five load scenarios as defined in Table 4 are given in order as ○, △, ×, ◇, □ for (a) wind speed (black), (b) current speed (red) and wave-induced velocity (green) and (c) for combined moment (black).

percentile mean load is around 29% of the combined system's peak bending moment (98.38 MNm), the reduction in peak load seen by the combined system if deployed at location 15 instead of location 1 would be less than 1% which is likely to be less than the accuracy of the model. As such there would be little benefit in terms of peak (design) moment reduction by placing a co-located structure at location 15 over location 1.

Table 4
Environmental conditions during operation at near-to -rated and -shutdown speeds for each the wind and tidal turbine located at location 1. For the wind turbine, near-to -rated operation is defined as $11 < U_{w_{rate}} < 20$ m/s and -shutdown as $20 \leq U_{w_{shut}} < 25$ in order to increase the number of samples. Similarly, for the tidal turbine near-to -rated operation is defined as $2.3 < U_{rate} < 3$ m/s and -shutdown as $3 \leq U_{shutdown} < 5$ m/s. For these 4 cases, $H_s < 3$ m was considered. $^{+}$The final shutdown-shutdown case is the extreme case of both turbines parked in shutdown and with $H_s > 3$ m.

Wind Turbine:	Rated	Rated	near-Shutdown	near-Shutdown	Shutdown
Tidal Turbine:	Rated	near-Shutdown	Rated	near-Shutdown	Shutdown^{+}
	(max-min)	(max-min)	(max-min)	(max-min)	(max-min)
$\|M\|$, MNm	82.42 – 12.71	98.38 – 95.80	68.88 – 17.42	88.41 – 67.22	95.43 – 23.31
U_w (90 m), m/s	11.38 – 16.67	11.75 – 16.01	21.90 – 20.19	20.18 – 21.94	32.76 – 25.18
U_c (mid-depth), m/s	2.86 – 2.65	4.40 – 3.56	2.93 – 2.58	3.85 – 3.19	2.73 – 2.50
U_{wav} (mid-depth), m/s	0.21 – 0.01	0.18 – 0.01	0.50 – 0.00	0.61 – 0.23	0.88 – 0.00
H_s	1.70 – 0.59	1.34 – 0.58	2.81 – 2.70	2.96 – 1.85	3.96 – 3.53^{+}
T_p	12.20 – 7.30	8.81 – 7.30	11.28 – 13.75	12.67 – 11.28	12.60 – 12.43
θ_w, °N	150 – 274	149 – 280	90 – 94	84 – 97	116 – 97
θ_c, °N	111 – 110	111 – 113	113 – 286	112 – 111	111 – 287
θ_{wav}, °N	129 – 73	124 – 73	131 – 129	130 – 129	129 – 129

7. Conclusions

The potential for increasing energy yield from tidal energy sites by co-deployment of wind and tidal turbines has been assessed in terms of the magnitude and variability of energy supply and the loading of support structures. The site considered is located in the Inner Sound of the Pentland Firth. A standard modelling approach is used for wind farm energy yield prediction and a turbine wake superposition model presented for the tidal farm energy yield. The influence of yaw strategy on tidal farm energy yield was considered and a slack-tide yaw strategy found to generate 2.6 times greater energy yield than a fixed yaw system and only 10% less than the yield available from a continuous system whilst offering a simpler mechanism. The sensitivity to a wave shutdown criterion was also investigated for a seven month period indicating that constraining operation to significant wave height less than 2.5 m reduced energy yield by 5%. A more onerous reduction is likely at more exposed sites.

Energy yield for the co-located array of four wind turbines and twenty tidal turbines was found to be 70% greater than for the tidal array alone. Monthly moving averages of the time varying power for the 3.5 year period exhibited large seasonal variations for the wind farm, although these generally followed UK power demand. In contrast, the tidal power variation at this temporal scale

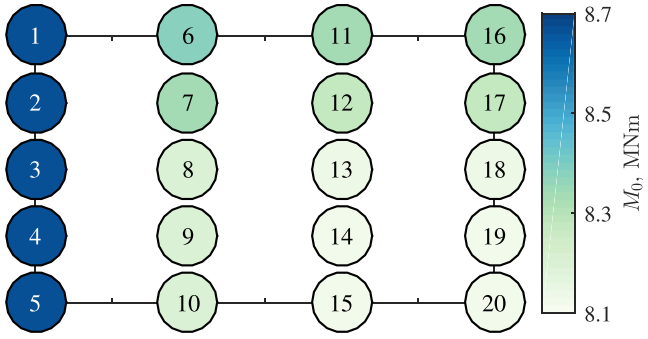

Fig. 21. Variation in logarithmic temporal-mean overturning moment for each tidal turbine location (1–20) across the array.

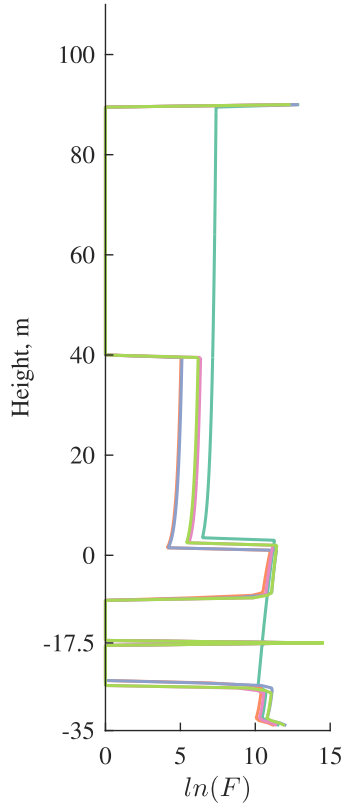

Fig. 20. Variation in force per unit length with height of the combined structure for the 5 cases of Table 4. Case 1, case 2, case 3, case 4, case 5.

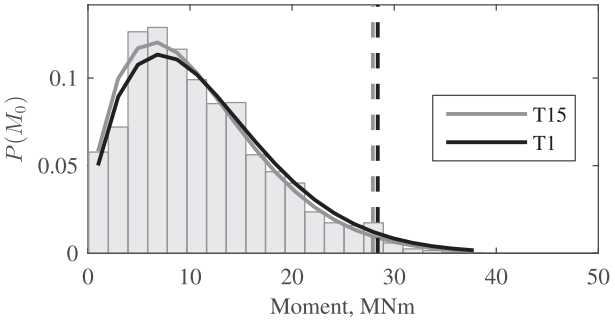

Fig. 22. Probability distributions of the overturning moments for tidal turbines only with maximum (black) and minimum (grey) mean loads across the array and corresponding 98th percentiles (dashed lines). Histogram shown for turbine number 15 only.

remained fairly constant with seasonal variation associated with wind power only.

Support structure loads due to wind, waves and current have been modelled to assess the loading on a structure supporting both a wind and tidal turbine relative to either turbine alone. Five load conditions are identified with maximum load occurring with wind operating at close to rated-speed and the tidal turbine close to its shutdown speed. However, the addition of a tidal turbine to a wind turbine support structure was found to have no significant impact on either mean or extreme overturning moment due to the larger moment arm of the wind turbine compared to that of the tidal turbine. This also meant that despite a 2% variation in loads across the tidal-only array, this would make negligible impact to loads on a co-located support structure and so there would be little structural advantage by situating co-located supports in these more sheltered tidal locations.

Co-deployment of wind turbines with 60% of the capacity of a tidal turbine farm results in 70% greater energy yield than a tidal farm of the same configuration and a reduced variability of power supply. Such deployment would involve shared support structures with design loads similar to wind turbine loading substituting tidal turbine support structures at one-fifth of the positions in the array. The prospect of attaining higher yield for reduced infrastructure is encouraging and further analysis is required of the extent to which commonality of infrastructure, installation processes and power export affects the economics of such co-located projects.

Acknowledgements

This work was jointly funded by the Engineering and Physical Sciences Research Council (Doctoral Training Partnership EP/K502947/1) and University of Manchester Alumni Research Impact Scholarship. The authors also thank Thomas Adcock (University of Oxford) for providing the ADCIRC model tidal current data and Philippe Gleizon (University of Highlands and Islands, Thurso) for providing wave buoy data of the Pentland Firth. Sources for all of the data used in this work are given in the text and all data resulting from analysis is presented.

References

[1] UNFCCC Conference of the Parties, Adoption of the Paris Agreement, 2015.
[2] DECC (Department of Energy & Climate Change), UK Energy Statistics, 2015 & Q4 2015, Tech. Rep, March, 2016.
[3] C. Willow, B. Valpy, J. Weston, RenewableUK - Building an Industry, Tech. Rep. June, BVG Associates, 2013.
[4] P. Heptonstall, R. Gross, P. Greenacre, T. Cockerill, The cost of offshore wind: understanding the past and projecting the future, Energy Policy 41 (2012) 815–821.
[5] G. Tina, S. Gagliano, S. Raiti, Hybrid solar/wind power system probabilistic modelling for long-term performance assessment, Sol. Energy 80 (5) (2006) 578–588.
[6] Z. Gao, T. Moan, L. Wan, C. Michailides, Comparative experimental study of the survivability of a combined wind and wave energy converter in two testing facilities, Ocean Eng. 111 (1) (2016) 82–94.
[7] Black and Veatch, Phase II - UK Tidal Stream Energy Resource Assessment, Tech. Rep. 0, Black and Veatch Consulting Ltd, 2005.
[8] T.A.A. Adcock, S. Draper, G.T. Houlsby, A.G.L. Borthwick, S. Serhadllu, The available power from tidal stream turbines in the Pentland Firth, Proc. Royal Soc. A Math. Phys. Eng. Sci. 469 (2157) (2013).
[9] A. Truewind, Openwind User Manual, October, 2012.
[10] J.F. Ainslie, Calculating the flowfield in the wake of wind turbines, J. Wind Eng. Ind. Aerod. 27 (1988) 213–224.
[11] N.G. Mortensen, 46200 Planning and Development of Wind Farms : Wind Resource Assessment Using the WAsP Software, Tech. Rep. December, Technical University of Denmark, 2014.
[12] Met Office, Operational NWP (Numerical Weather Prediction) Output from the Met Office Unified Model (UM) - Oct. 2000-Jan. 2012 Only, 2013.
[13] H. Santo, P.H. Taylor, R.E. Taylor, P. Stansby, Decadal variability of wave power production in the North-East Atlantic and North Sea for the M4 machine, Renew. Energy 91 (2016) 442–450.
[14] W. Skamarock, J. Klemp, J. Dudhi, D. Gill, D. Barker, M. Duda, X.-Y. Huang, W. Wang, J. Powers, A Description of the Advanced Research WRF Version 3, Tech. Rep. June, National Center for Atmospheric Research, Boulder, Colorado, 2008.
[15] G. Cuevas-Figueroa, Prediction of Energy Production from Wind Farms with Case Study of Baja California (Ph.D. thesis), University of Manchester, 2016.
[16] A. Saruwatari, D.M. Ingram, L. Cradden, Wave-current interaction effects on marine energy converters, Ocean. Eng. 73 (2013) 106–118.
[17] NCEP, NCEP FNL Operational Model Global Tropospheric Analyses, Continuing from July 1999, 2000.
[18] S. Caires, A. Sterl, A new nonparametric method to correct model data: application to significant wave height from the ERA-40 re-analysis, J. Atmos. Ocean. Technol. 22 (4) (2005) 443–459.
[19] S. Draper, A.G.L. Borthwick, G.T. Houlsby, Energy potential of a tidal fence deployed near a coastal headland Energy potential of a tidal fence deployed near a coastal headland, Phil. Trans. R. Soc. A 371 (1985) (2013) 1–16.
[20] M. Edmunds, R. Malki, A.J. Williams, I. Masters, T. Croft, Aspects of tidal stream turbine modelling in the natural environment using a coupled BEM - CFD model, Int. J. Mar. Energy 7 (2014) 20–42.
[21] A. Olczak, T. Stallard, T. Feng, P. Stansby, Comparison of a RANS blade element model for tidal turbine arrays with laboratory scale measurements of wake velocity and rotor thrust, J. Fluids Struct. 64 (2016) 87–106.
[22] N. Jensen, A Note on Wind Generator Interaction, Tech. Rep., Risø, 1983.
[23] S. G. Parkinson, T. Stallard, M. Thomson, A. Wickham, R. Willden, Comparison of scale model wake data with an energy yield analysis tool for tidal turbine farms, in: International Conference on Ocean Energy, 2–6, 2012.
[24] T. Stallard, T. Feng, P. Stansby, Experimental study of the mean wake of a tidal stream rotor in a shallow turbulent flow, J. Fluids Struct. 54 (2014) 235–246.
[25] P. Stansby, T. Stallard, Fast optimisation of tidal stream turbine positions for power generation in small arrays with low blockage based on superposition of self-similar far-wake velocity deficit profiles, Renew. Energy 92 (2016) 366–375.
[26] D. Sudall, A. Olczak, T. Stallard, P. Stansby, Simplified wake models for small tidal farms : reduced scale evaluation and array loading study, in: 4th Oxford Tidal Energy Workshop, March 2016, vols. 8–10, 2015.
[27] E. Blockley, J. Siddorn, B. Hackett, N. McConnell, A. Hines, Product User Manual for North-West Shelf Physical Forecast Product, Tech. Rep. 3, UK Met Office, 2015.
[28] D. Sudall, P. Stansby, T. Stallard, Energy yield for collocated offshore wind and tidal stream farms, in: EWEA Offshore, 2015, pp. 1–10.
[29] J. Hardwick, I. Ashton, L. Johanning, Field characterisation of currents and near surface eddies in the Pentland Firth, in: 4th Oxford Tidal Energy Workshop, March, 34–35, 2015.
[30] DECC, Digest of UK Energy Statistics (DUKES) Chapter 6, Tech. Rep., 2014.
[31] TEL, DeltaStream Tidal Energy Solution - a Tidal Energy White Paper, Tech. Rep., August, 2012.
[32] J. McNaughton, S. Harper, R. Sinclair, B. Sellar, Measuring and modelling the power curve of a commercial-scale tidal turbine, in: Proceedings of 11th European Wave and Tidal Energy Conference, Nantes, France, 2015, pp. 1–92015.
[33] P. Fraenkel, Development and testing of marine current Turbine's SeaGen 1.2MW tidal stream turbine, 3rd International Conference on Ocean Energy (2010) 1–72010.
[34] J. McNaughton, Turbulence Modelling in the Near-field of an Axial Flow Tidal Turbine Using Code_Staturne (Ph.D. thesis), University of Manchester, 2013.
[35] EMEC, Marine Renewable Energy Guides - Assessment of Tidal Energy Resource, Tech. Rep., BSI, 2009.
[36] DNV, DNV-OS-J101 Design of Offshore Wind Turbine Structures, 2013.
[37] DNV GL, DNVGL-ST-0164 Tidal Turbines, 2015.
[38] L. Goddijn-Murphy, D.K. Woolf, M.C. Easton, Current patterns in the inner sound (Pentland Firth) from underway ADCP data, J. Atmos. Ocean. Technol. 30 (2013) 96–111.
[39] E.ON, Rampion Offshore Wind Farm Draft Environmental Statement, Tech. Rep., 2012.
[40] DNV, DNV-OS-J101 Design of Offshore Wind Turbine Structures, 2013.
[41] BSI, BS EN 1993-3-1:2006 Eurocode 3 Design of Steel Structures, Tech. Rep, July, 2009.
[42] T. Burton, D. Sharpe, N. Jenkins, E. Bossanyi, Wind Energy Handbook, Wiley, 2001.
[43] DNV, DNV-RP-C205 Environmental Conditions and Environmental Loads, 2014.
[44] BSI, BS EN 61400-3:2009 Wind Turbines - Part 3: Design Requirements for Offshore Wind Turbines, 2009.
[45] M. Turk, S. Emeis, The dependence of offshore turbulence intensity on wind speed, J. Wind Eng. Ind. Aerod. 98 (8–9) (2010) 466–471.
[46] A. Westerhellweg, B. Canadillas, T. Neumann, Direction dependency of offshore turbulence intensity in the German bight, in: 10th Wind Energy Conference DEWEK, vol. 2, 2010, pp. 3–7.
[47] BSI, BS EN 61400-1:2005 +A1:2010 Wind Turbines Part 1: Design Requirements, Tech. Rep., IEC, 2010.
[48] K.S. Hansen, G.C. Larsen, Characterising turbulence intensity for fatigue load analysis of wind turbines, Wind Eng. 29 (4) (2005) 319–329.
[49] T. Sarpkaya, Force on a circular cylinder in viscous oscillatory flow at low KeuleganCarpenter numbers, J. Fluid Mech. 165 (1986) 61.
[51] D. R. J. Sutherland, B. G. Sellar, S. Harding, I. Bryden, Initial flow characterisation utilising turbine and seabed installed acoustic sensor arrays, in: 10th

European Wave and Tidal Energy Conference, Aalborg, Denmark, 2013.
[52] E. Osalusi, J. Side, R. Harris, Structure of turbulent flow in EMEC's tidal energy test site, Int. Commun. Heat Mass Transf. 36 (5) (2009) 422–431.
[53] J. Thomson, B. Polagye, V. Durgesh, M.C. Richmond, Measurements of turbulence at two tidal energy sites in puget sound, WA, J. Ocean. Eng. 37 (3) (2012) 363–374.
[54] G.Z. Simeón, C.B. Ferreira, Identification of the uncertainties for the calibration of the partial safety factors for load in tidal turbines, J. Mar. Sci. Eng. 4 (20) (2016).
[55] A. Olczak, The Influence of Waves on Tidal Stream Turbine Arrays (Ph.D. thesis), University of Manchester, 2015.
[56] G. Buss, P. Stansby, SAWW, Steady Arbitrary Water Waves a Computer Program to Compute the Properties of Steady Water Waves, Tech. Rep., University of Manchester, 1982.
[57] M.M. Rienecker, J.D. Fenton, A Fourier approximation method for steady water waves, J. Fluid Mech. 104 (1981) 119.
[58] P.K. Stansby, L.C. Devaney, T.J. Stallard, Breaking wave loads on monopiles for offshore wind turbines and estimation of extreme overturning moment, IET Renew. Power Gener. 7 (5) (2013) 514–520.
[59] S. Caires, M.V. Gent, Wave height distribution in constant and finite depths, in: Proceedings of 33rd Conference on Coastal Engineering, Santander, 2012.
[60] E. Fernandez-Rodriguez, T. Stallard, P. Stansby, Experimental study of extreme thrust on a tidal stream rotor due to turbulent flow and with opposing waves, J. Fluids Struct. 51 (2014) 354–361.
[61] E. Fernandez-Rodriguez, Analysis of Floating Support Structures for Marine and Wind Energy (Ph.D. thesis), University of Manchester, 2014.
[62] A.M. Foley, P.G. Leahy, A. Marvuglia, E.J. Mckeogh, Current methods and advances in forecasting of wind power generation, Renew. Energy 37 (1) (2012) 1–8.